Signal Processing: *Image Communication* 25 (2010) 28–46

Contents lists available at ScienceDirect

Signal Processing: *Image Communication*

journal homepage: www.elsevier.com/locate/image

A study of relative phase in complex wavelet domain: Property, statistics and applications in texture image retrieval and segmentation

An Vo *, Soontorn Oraintara

Department of Electrical Engineering, University of Texas at Arlington, Arlington, TX 76019, USA

ARTICLE INFO

Article history:
Received 7 November 2008
Received in revised form
14 August 2009
Accepted 20 September 2009

Keywords:
Relative phase
Statistics of relative phase
Pdf of relative phase
Statistical image modeling
Von Mises distribution
Wrapped Cauchy distribution
Pyramidal dual-tree directional filter bank
Dual-tree complex wavelet transform
Uniform discrete curvelet transform
Texture image retrieval
Texture segmentation

ABSTRACT

In this paper, we develop a new approach which exploits the probabilistic properties from the phase information of 2-D complex wavelet coefficients for image modeling. Instead of directly using phases of complex wavelet coefficients, we demonstrate why relative phases should be used. The definition, properties and statistics of relative phases of complex coefficients are studied in detail. We proposed von Mises and wrapped Cauchy for the probability density function (pdf) of relative phases in the complex wavelet domain. The maximum-likelihood method is used to estimate two parameters of von Mises and wrapped Cauchy. We demonstrate that the von Mises and wrapped Cauchy fit well with real data obtained from various real images including texture images as well as standard images. The von Mises and wrapped Cauchy models are compared, and the simulation results show that the wrapped Cauchy fits well with the peaky and heavy-tailed pdf of relative phases and the von Mises fits well with the pdf which is in Gaussian shape. For most of the test images, the wrapped Cauchy model is more accurate than the von Mises model, when images are decomposed by different complex wavelet transforms including dual-tree complex wavelet (DTCWT), pyramidal dual-tree directional filter bank (PDTDFB) and uniform discrete curvelet transform (UDCT). Moreover, the relative phase is applied to obtain new features for texture image retrieval and segmentation applications. Instead of using only real or magnitude coefficients, the new approach uses a feature in which phase information is incorporated, yielding a higher accuracy in texture image retrieval as well as in segmentation. The relative phase information which is complementary to the magnitude is a promising approach in image processing.

1. Introduction

It is well known that an advantage of complex wavelets compared to conventional real-valued wavelets is that they provide both magnitude and phase information. The magnitude of a complex coefficient describes the strength of feature such as edges while the phase indicates the location of the feature. In many image processing applications, only the real part or the magnitude of complex wavelet coefficient and its statistical model are used, although the phase information can hold important statistical properties of the image. The property and statistical model of phase and its benefits have not been studied deeply. An essential question raised is how to efficiently utilize the phase information of complex wavelet coefficients for image modeling. In this paper, we develop a new approach to exploit the statistical properties from the phase information of 2-D complex wavelet coefficients of an image.

* Corresponding author.
E-mail address: anphuocnhu.vo@mavs.uta.edu (A. Vo).
URL: http://www.naaan.org/anvo/ (A. Vo).

0923-5965/$ - see front matter © 2009 Elsevier B.V. All rights reserved.
doi:10.1016/j.image.2009.09.003

There have been several works on the statistics of real coefficients of the wavelet transform [1,2]. The wavelet coefficients within a subband which have the peaky and heavy-tailed non-Gaussian distribution can be modeled by a two-parameter generalized Gaussian density (GGD) [1,3,4]. The GGD is applied to image denoising as a prior density and outperforms the Gaussian model [3–5]. Although the GGD wavelet marginal model is more powerful than the Gaussian model, it does not take into account the dependencies between different subbands as well as between a coefficient and its neighboring coefficients in the same subband.

Various researchers have developed joint statistical models in the wavelet domain [6–9]. A bivariate probability density function has been proposed to model the statistical dependencies between a wavelet coefficient and its parent [9]. The hidden Markov model with a two-state hidden multiplier variable was introduced in [6,7] to capture the key features of the joint probability density of the wavelet coefficients. A continuous multiplier variable has been proposed to govern the local variance [8,10–12]. In [8,13], the authors developed a model for the neighborhoods of oriented pyramid coefficients based on a Gaussian scale mixture (GSM) which is the product of a Gaussian random vector and an independent hidden random scalar multiplier. The GSM estimator provides significantly higher performances in terms of both mean square error and visual quality in image denoising [13]. In most of the above statistical models, only the real part of coefficients is modeled.

In [14–17], the magnitude distribution of the dual-tree complex wavelet transform (DTCWT) coefficients is modeled by a scaled mixture of Rayleigh distribution. However, in [18], the authors show that for a Gaussian distributed signal, the magnitude distribution of the DTCWT coefficients can be modeled by the Rayleigh distribution for only the second and higher level decompositions and by the generalized Gamma for the first-level decomposition. In [18], the density function of the phase components is not uniform for the first-level decomposition, and it is uniform for the second and higher level decompositions. Therefore, the moments of the phase distribution are computed. However, for natural images, distribution of phase components is uniform in all subbands of complex wavelet transforms such as the pyramidal dual-tree directional filter bank (PDTDFB) [19] and the uniform discrete curvelet transform [20].

In some applications a knowledge of the statistical properties of phase components is used, such as edge detection [21], image painting and reconstruction [22,23]. Some other applications exploit the local phase information across scales of the complex wavelet such as the description of texture images [12], the detection of blurred images [24], object recognition [25] and the face recognition [26]. In [12] the local phase behavior is captured by the cross-correlation of complex coefficients of bands at adjacent scales (fine-scale and coarse-scale), and this statistical measurement distinguishes edges from lines and helps in representing gradients due to shading and lighting effects. In [24], the local phase coherence relationship across scale and space has been suggested and the phases of the finest scale coefficients can be well predicted from those of the coarser scale coefficients. The disruption of this local phase is an effective measure for blur detection. This across scale relationships are also captured using modified product of coefficients at adjacent scales and have been used in [25,27]. Another investigation of local phase in the same orientation and the same scale is based on the DTCWT and the feature orientations are determined by the phase difference between the adjacent coefficients in six fixed directional subbands [28].

A statistical model for phases of complex wavelet coefficients has not been explicitly utilized in image processing applications. Therefore, our proposed model in this work can be beneficial to the image processing community. In this paper, we develop a new studying approach of phase difference of two neighboring complex wavelet coefficients called relative phase. The statistics of relative phase are studied. Two simple periodic distributions, the von Mises and wrapped Cauchy are proposed to capture the relative phase statistics. The parameters of both models are estimated by maximizing the likelihood function. We compare the performances of two models using real images which include the standard and texture images.

The remainder of this paper is organized as follows. The complex wavelet transforms are reviewed in Section 2. We study the property of relative phases in Section 3. The statistics of relative phases in the complex wavelet domain are observed, and the von Mises and wrapped Cauchy distributions are proposed for modeling relative phases in Section 4. A comparison of the von Mises with the wrapped Cauchy for relative phases in different complex wavelet transforms is also presented in Section 4. Finally, by combining the magnitude and phase of complex coefficients, new feature vectors are proposed to discriminate textures in texture image retrieval in Section 5 and texture segmentation in Section 6. The data and scripts used in this study are available at http://www.naaan.org/anvo.

2. A review of complex wavelet transforms

The main advantages of the complex wavelet transform over the discrete wavelet transform (DWT) are its shift invariant property and good directional selectivity [29]. The complex wavelet transform is suitable for many applications of interest in image communication such as coding [30], denoising [9,31], motion estimation [32], quality measures [33], and image retrieval [34]. In this section, a brief review of various complex wavelet transforms is presented.

Each pair of complex filters has the Hilbert transform relationship. Therefore, the equivalent directional complex filter for each subband has a one-sided frequency support, as illustrated in Figs. 2(a) and 3(b). In spatial domain, the real part of the complex filter is symmetric while the imaginary part is anti-symmetric. The amplitude and phase information of complex coefficients

provide local information on the directional feature of image at a specific scale and direction.

2.1. The dual-tree complex wavelet transform

The dual-tree complex wavelet transform (DTCWT) [35,36] has been proposed by Kingsbury. Its filters employed in the two trees are designed in such a way that the aliasing in one branch in the first tree is approximately canceled by the corresponding branch in the second tree. The design of the DTCWT in [36] focuses on the design of a two-channel FB having filters satisfying the half-sample phase delay condition with respect to an existing FB. Directional selectivity is achieved in the 2-D case by combining the outputs of the FB in such a way that the equivalent complex filters have supports in only one quadrant of the frequency plane [35]. This method of increasing directionality is equivalent to attaching quadrant FBs [37] to the highpass subband of the DWT. The DTCWT with six directional subbands is better than the DWT with four subbands in directional selectivity. We refer to [29] for an excellent tutorial overview on the DTCWT. In this paper, we will use the DTCWT in Sections 4–6.

2.2. Pyramidal dual-tree directional filter banks

The pyramidal dual-tree directional filter bank (PDTDFB) shown in Fig. 1(a) has been introduced in [19]. Each resolution level consists of a two-channel FB and a pair of directional filter banks (DFBs). The purpose of the PDTDFB is to provide a shiftable and scalable multiresolution directional decomposition. An example of the frequency supports of a three-level eight-band PDTDFB is shown in Fig. 2. This transform has some similarities with the complex version of the shiftable pyramid [38], while maintaining a much lower redundant ratio. The PDTDFB can have 2^n directional subbands, where $n \geq 1$.

According to Fig. 1(a), the input image is first filtered by the lowpass filter $L_0(\mathbf{z})$, while the narrow band highpass information (R_0) is disregarded, before passing through the first level of a multiresolution FB. This two-channel FB has two filters, highpass $R_1(\mathbf{z})$ and lowpass $L_1(\mathbf{z})$. Slices of the frequency responses of these filters at $\omega_2 = 0$ are illustrated in Figs. 1(b) and (c). The high frequency component at the output of the filter $R_1(\mathbf{z})$ is then decomposed by the pair of primal and dual DFBs, resulting in the highest resolution directional decomposition. The low frequency component, after decimation by $\mathbf{D}_2 = 2\mathbf{I}$, is fed into the second level decomposition for the second resolution. The block P shows one level of the PDTDFB, where the 2×2^n decimated outputs of the two DFBs are the real and imaginary parts of 2^n complex-valued subbands. For more details of the construction of the PDTDFB, the reader is referred to [19]. The PDTDFB will be used in Sections 4–6.

2.3. Uniform discrete curvelet transform

The uniform discrete curvelet transform (UDCT) borrows the ideas from two recently introduced discrete transforms, which are the PDTDFB [19] and the fast discrete curvelet transform (FDCT) [39]. Similar to the DTCWT and PDTDFB, the directional filters have one-sided support in the frequency domain, making the subband coefficients complex. The same transform with different values of M and N is applied iteratively at the lowpass subband to create a multiresolution decomposition. In the reconstruction procedure, the final complex components

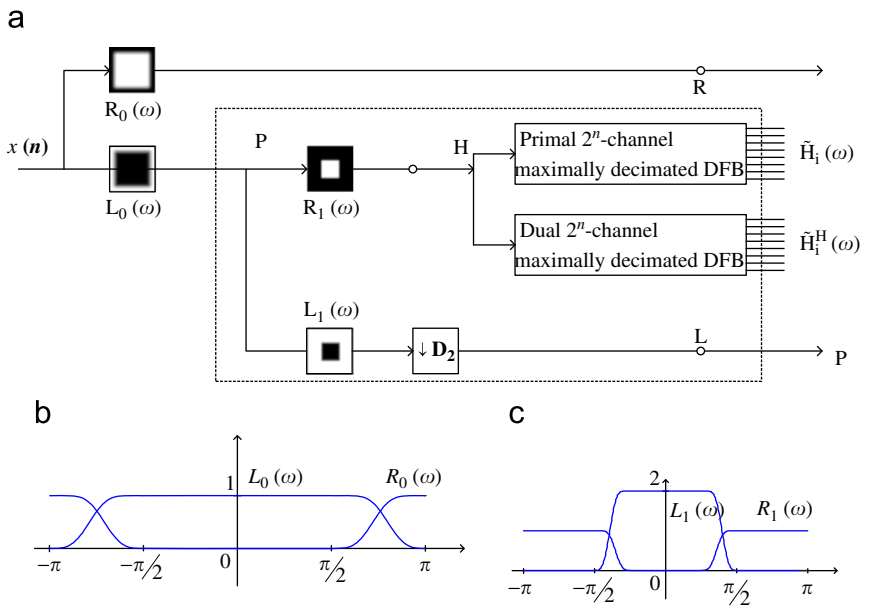

Fig. 1. (a) The FB implemented the pyramidal PDTDFB image representation. The block P is reiterated to create multi-level decomposition. Slices of the 2-D frequency responses of: (b) $R_0(\mathbf{z})$ and $L_0(\mathbf{z})$, and (c) $R_1(\mathbf{z})$ and $L_1(\mathbf{z})$.

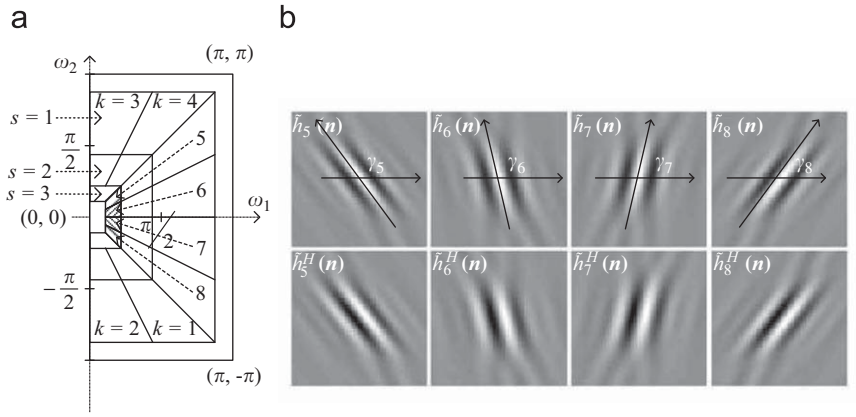

Fig. 2. The essential frequency supports of (a) the complex filters in the three-level eight-band PDTDFB decomposition, and (b) corresponding spatial impulse responses.

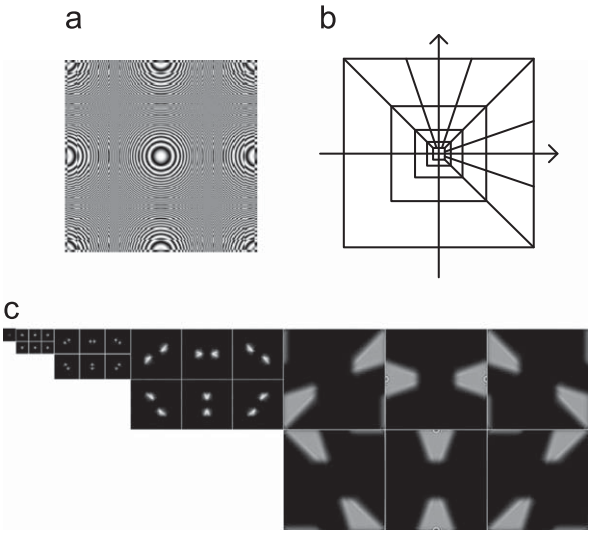

Fig. 3. (a) The zoneplate image, (b) frequency support of the curvelet functions, and (c) magnitude of complex coefficients in the transform domain with four scales and six orientations.

are simply discarded. We can interpret this as a dual-tree FB structure [36].

The discrete transform also has some similarities to the wrapping-based fast discrete curvelet transform [39] in the sense that both are defined based on windowing in the DFT domain. The main difference is that in the wrapping-based FDCT, the redundancy of transform is reduced by wrapping the frequency domain of subbands, while in the implementation, the redundancy is reduced by decimating the subbands by diagonal integer matrices. By this construction, the UDCT basis functions are located on a uniform integer grid at each resolution, while the basis of the FDCT is located on a non-integer grid. Fig. 3 is an example of the zoneplate image decomposed by the UDCT. The decomposition has four directional scales, with $N = 6$ at each scale. Fig. 3(c) shows the magnitude of the complex coefficients in the transform domain. In general, the UDCT can have 3×2^n directional subbands, where $n \geq 0$. For the detailed construction of the UDCT, the reader is referred to [20]. In this paper, the UDCT will be used in Sections 4 and 5.

3. Relative phase in complex wavelet domain

3.1. Linear relationship between local phase and distance

It has been stated in [12] that the local phase varies linearly with the distance from features and in [28], the authors also have observed that the phase of a 1-D DTCWT coefficient is consistently linear with respect to the feature offset (distance to the step). However, the proof for this relationship has not been given. Here, we will show that the phase in the vicinity of the feature such as a step or a ramp has a linear relationship with the distance.

Let the input $x(t) = u(t)$ be a unit step signal, and the ideal complex filter $h(t)$ has one-sided frequency support $H(\omega)$ as

$$H(\omega) = \begin{cases} 1 & 0 \leq \omega_1 \leq \omega \leq \omega_2, \\ 0 & \text{otherwise.} \end{cases} \tag{1}$$

The output $y(t)$ can be expressed as

$$\begin{aligned} y(t) &= \frac{1}{2\pi}\int_{-\infty}^{\infty} H(\omega)X(\omega)e^{j\omega t}\,d\omega = \frac{1}{2\pi}\int_{\omega_1}^{\omega_2} \frac{1}{j\omega}e^{j\omega t}\,d\omega \\ &= \frac{1}{2\pi}\int_{\omega_1}^{\omega_2} \frac{1}{j\omega}\sum_{n=0}^{\infty}\frac{(j\omega t)^n}{n!}\,d\omega \\ &= \frac{1}{2\pi j}\left(\ln\left|\frac{\omega_2}{\omega_1}\right| + \sum_{n=1}^{\infty}\frac{(jt\omega_2)^n - (jt\omega_1)^n}{n!n}\right). \end{aligned}$$

Because the output $y(t)$ is considered in the vicinity of the step, i.e. $|\omega t| \ll 1$, hence $y(t)$ can be approximated by

$$y(t) \approx \frac{1}{2\pi j}\left(\ln\left|\frac{\omega_2}{\omega_1}\right| + jt(\omega_2 - \omega_1)\right),$$

and the phase of $y(t)$ can be approximated by

$$\angle y(t) \approx \tan^{-1}\left(\frac{\omega_2-\omega_1}{\ln\left|\frac{\omega_2}{\omega_1}\right|}t\right)-\frac{\pi}{2}$$

$$=\tan^{-1}\left(\frac{\omega_2\left(1-\frac{\omega_1}{\omega_2}\right)}{\ln\left|\left(\frac{\omega_1}{\omega_2}\right)^{-1}\right|}t\right)-\frac{\pi}{2}.$$

Let $p=1-\omega_1/\omega_2$. Hence $p\in[0\ 1]$. In addition, we have the inequality: $1-p\le e^{-p}$ for $0\le p\le 1$. Therefore,

$$\frac{\omega_2\left(1-\frac{\omega_1}{\omega_2}\right)t}{\ln\left|\left(\frac{\omega_1}{\omega_2}\right)^{-1}\right|}=\frac{\omega_2 pt}{\ln|(1-p)^{-1}|}\le\frac{\omega_2 pt}{\ln|e^{p}|}=\omega_2 t\ll 1,$$

and the phase of $y(t)$ can be approximated by

$$\angle y(t)\approx\left(\frac{\omega_2-\omega_1}{\ln\left|\frac{\omega_2}{\omega_1}\right|}\right)t-\frac{\pi}{2}.$$

Similarly, let the input $x(t)=tu(t)$ be a unit ramp signal and the ideal complex filter $H(\omega)$ be defined as above. In this case, the phase of $y(t)$ can be approximated by

$$\angle y(t)\approx\tan^{-1}\left(\frac{\omega_1\omega_2\ln\left|\frac{\omega_2}{\omega_1}\right|}{\omega_2-\omega_1}t\right)\approx\left(\frac{\omega_1\omega_2\ln\left|\frac{\omega_2}{\omega_1}\right|}{\omega_2-\omega_1}\right)t.$$

From the above formula, the phase of $y(t)$ in the vicinity of features such as steps or ramps (at $t=0$) is linear with t (the distance to feature).

3.2. Relative phase and its property

In this section, we study the relationship between angle of an edge and local phases in the PDTDFB domain, from which we define relative phase and state its property in the complex wavelet domain.

Let us consider an edge at angle α_k in the supported region of the PDTDFB subband k. The center angle of subband k is γ_k. Assume that the two horizontally adjacent coefficients A and B are located in the neighborhood of an edge. AA' and BB' represent the distances from A and B to the edge in the direction normal to subband orientation, respectively. The distance between A and B at scale s is $D_s=2^s$. The feature orientation or the angle of the edge α_k can be approximated by

$$\alpha_k\approx\begin{cases}\gamma_k-\tan\gamma_k+\dfrac{AA'-BB'}{D_s\cos\gamma_k} & \text{if } 1\le k\le\dfrac{K}{4},\\ \gamma_k-\tan\gamma_k-\dfrac{AA'-BB'}{D_s\cos\gamma_k} & \text{if } \dfrac{K}{4}<k\le\dfrac{K}{2},\\ \gamma_k+\cot\gamma_k+\dfrac{AA'-BB'}{D_s\sin\gamma_k} & \text{if } \dfrac{K}{2}<k\le\dfrac{3K}{4},\\ \gamma_k+\cot\gamma_k-\dfrac{AA'-BB'}{D_s\sin\gamma_k} & \text{if } \dfrac{3K}{4}<k\le K.\end{cases}\quad(2)$$

In the 2-D case, the behavior of the phase is a straightforward extension of the 1-D case as shown in Section 3.1, Figs. 4(b) and (c) show the magnitude and phase of a PDTDFB coefficient at A (Fig. 4(a)) when the edge (angle $\alpha_k=135^\circ$) is translated from A_1 to A_2. The x-axis represents the translation distance of the edge in horizontal direction. When A lies on the edge, $x=0$. The distance from A to the edge is approximately $x\sin\alpha_k$. We observe that when the edge moves from A_1 to A_2, the corresponding phase at A (Fig. 4(c)) varies linearly with respect to the distance to the edge in the direction normal to the subband orientation (γ_k). Hence, the phase at A can be estimated by

$$\angle y_{sk}(A)=a_{sk}AA'+b_{sk}.\quad(3)$$

The slope a_{sk} and the intercept b_{sk} are constants for each scale s and orientation k. Therefore the term $(AA'-BB')$ in (2) can be computed from the difference of the phases at A and B:

$$AA'-BB'=\frac{\angle y_{sk}(A)-\angle y_{sk}(B)}{a_{sk}},\quad(4)$$

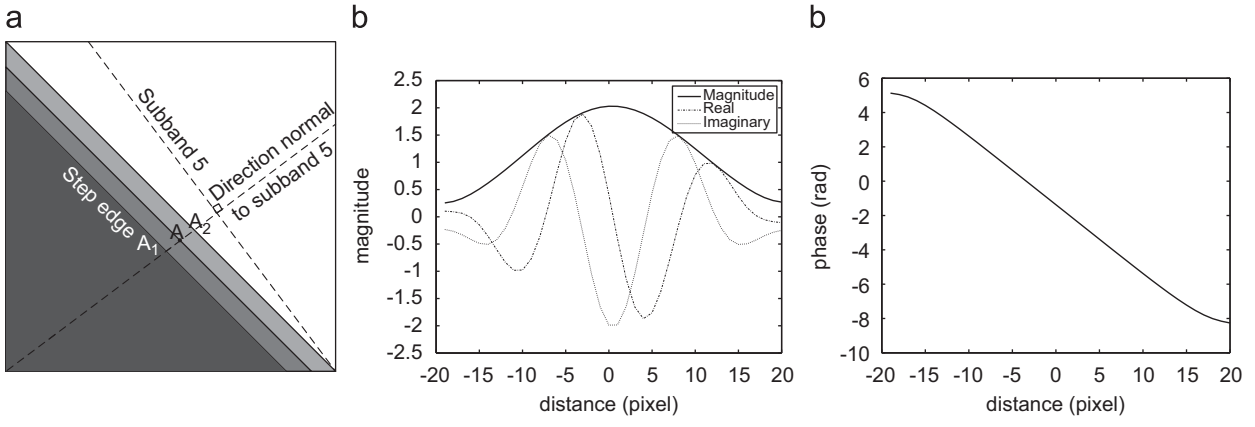

Fig. 4. Translation of an edge from A_1 to A_2 for subband $s=3$ and $k=5$ when $\alpha_k=135^\circ$: (a) edge translation, and coefficient at A for different positions of the edge: (b) magnitude and (c) phase.

when a_{sk} can be estimated from the phase data in Fig. 4(c). From (2) and (4), the feature orientation α_k of all PDTDFB subbands is linearly proportional to the term $(\angle y_{sk}(A) - \angle y_{sk}(B))$.

It is noted that to handle circularity of the phase $\angle y$ returns the phase angle, in radian, for complex coefficient y. The angles lie between $\pm\pi$.

Definition 3.1. The relative phase at a spatial location (i,j) within a particular complex subband is defined as the phase difference of two adjacent complex wavelet coefficients, e.g.,

$$\theta(i,j) = \angle y(i,j) - \angle y(i,j+1)$$

or

$$\theta(i,j) = \angle y(i,j) - \angle y(i+1,j), \tag{5}$$

where $y(i,j)$ is the coefficient at position (i,j).

Property 3.1. *The feature orientation α of an edge in the supported region of a subband is linearly proportional to the relative phase of two adjacent complex wavelet coefficients which are located in the vicinity of the edge as follows*:

$$\alpha \approx a + b\theta(i,j), \tag{6}$$

where a and b are constant and can be estimated for each subband.

It is noted that the PDTDFB is an example to prove the property of relative phase. This property also agrees with other complex wavelet transforms such as the DTCWT and the UDCT.

4. Statistics of relative phases in complex wavelet domain

In this section, we will observe behaviors of relative phase within a subband and propose its probability density functions.

4.1. Descriptive statistics

Since phase is circular data, we will need some measures like circular mean, circular variance to describe the circular distribution. These will be useful in making comparisons between circular distributions.

4.1.1. Measure of center and circular mean

Let $\theta_1, \theta_2, \ldots, \theta_n$ be a set of circular observations given in terms of angles. Consider the polar to rectangular transformation for each observation $(\cos\theta_i,\ \sin\theta_i)$, $i = 1,2,\ldots,n$. We obtain the resultant vector of these n unit vectors by summing them to get

$$R = (C,S) = \left(\sum_{i=1}^{n}\cos\theta_i, \sum_{i=1}^{n}\sin\theta_i\right). \tag{7}$$

The direction of this resultant vector R is the circular mean direction, denoted by $\overline{\theta}$ and defined as follows:

$$\overline{\theta} = \arg\left(\sum_{i=1}^{n}\cos\theta_i + j\sum_{i=1}^{n}\sin\theta_i\right). \tag{8}$$

So, the circular mean direction is given by

$$\overline{\theta} = \arctan\left(\frac{\sum_{i=1}^{n}\sin\theta_i}{\sum_{i=1}^{n}\cos\theta_i}\right), \tag{9}$$

where arctan is the four quadrant inverse tangent. Using function *atan2.m* in Matlab, we can find the four quadrant inverse tangent of the real parts of the elements of C and S, where $-\pi \le \overline{\theta} = \text{atan2}(S,C) \le \pi$.

4.1.2. Measure of dispersion and circular variance

The direction $\overline{\theta}$ of the vector resultant R provides a mean direction. However, we would like to know how concentrated circular data are towards this center. If all angles point in the same direction, the concentration is high. Conversely, if the data spread over the circle, there will be no concentration. The dispersion D of the points corresponding to θ_i on the unit circle is defined as

$$D = \frac{1}{n}\sum_{i=1}^{n}(1 - \cos(\theta_i - \alpha)), \tag{10}$$

where α is an angle of an arbitrary point on the unit circle.

The dispersion D will be minimized at $\alpha = \overline{\theta}$. The circular variance is defined as

$$S = 1 - \overline{R} = 1 - \frac{1}{n}\sum_{i=1}^{n}(1 - \cos(\theta_i - \overline{\theta})), \tag{11}$$

where $\overline{R}$ is the mean resultant length, and $0 \le S \le 1$. If the n observed directions are tightly clustered about the mean direction $\overline{\theta}$ then circular variance S will be nearly zero. On the other hand, if the directions are widely dispersed then S will be nearly one.

4.2. Circular probability distributions of relative phase

Our objective in this subsection is to find a statistical model which is able to capture the relative phase behaviors in the complex wavelet domain. The distribution for phases of complex coefficients is uniform as shown in Fig. 5(a). This uniform distribution of phases cannot yield any information of the image. Fig. 5(b) displays the histogram of the relative phase in one subband showing a (periodic) bell shape similar to the Gaussian distribution. Hence we propose the von Mises for modeling the probability density function (pdf) of the relative phase in the complex wavelet domain.

4.2.1. Von Mises distribution

An angular random variable θ has the von Mises distribution with the parameters μ and v $VM(\mu, v)$ [40,41] if its pdf has the form

$$p(\theta;\mu,v) = \frac{1}{2\pi I_0(v)}e^{v\cos(\theta-\mu)}, \tag{12}$$

where I_0 denotes the modified Bessel function of the first kind and the zero-th order which can be defined by $I_0(v) = (1/\pi)\int_0^{\pi} e^{v\cos\theta}\,d\theta$. The von Mises density functions in (12) with various values of v and μ are depicted in Fig. 6.

The parameter μ is the mean direction and the parameter v is known as the concentration parameter.

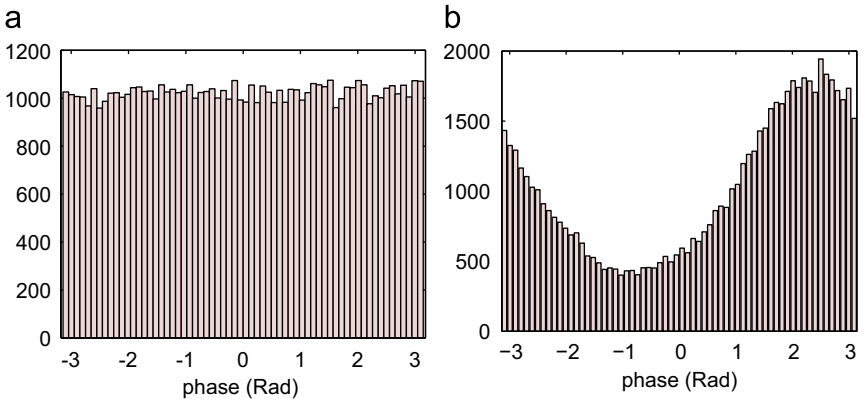

Fig. 5. Histograms at a particular wavelet subband of Barbara image: (a) phases of complex coefficients, (b) relative phase.

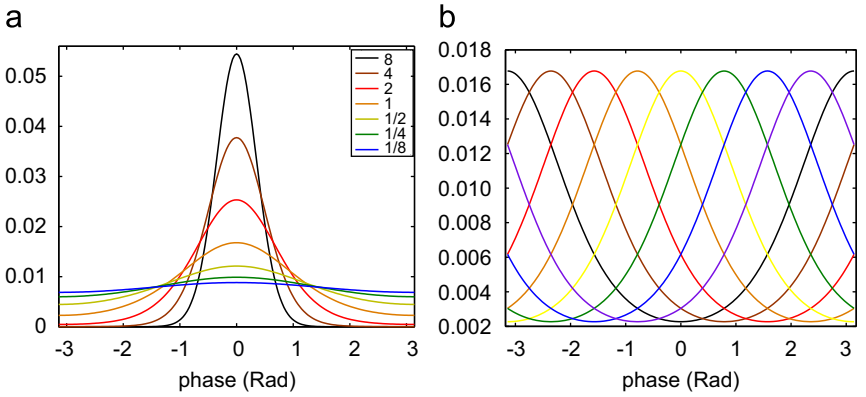

Fig. 6. Von Mises distributions: (a) $v=[\frac{1}{8},\frac{1}{4},\ldots,8]$ and $\mu=0$, (b) $v=1$ and $\mu=[-\pi,-3\pi/4,\ldots,3\pi/4]$.

Note that $VM(\mu,v)$ and $VM(\mu+\pi,-v)$ have the same distribution. For this model, we set the values of v to be non-negative, and the ranges of θ and μ are $[-\pi\ \pi]$. The VMs distribution is unimodal with two parameters μ and v, and is symmetrical about mean direction $\theta=\mu$. The larger the value of concentration parameter v, the denser the clustering around the mean direction μ. For $v=0$, the von Mises distribution tends to the uniform distribution. As $v\to\infty$ it becomes concentrated at the point $\theta=\mu_0$. The parameters of the von Mises distribution are estimated using maximum-likelihood as shown in Appendix A.

Fig. 8 shows the empirical histogram of the relative phase in a particular complex wavelet subband for four different natural images, along with the best fitting of the von Mises distribution. Fitting was performed by maximum-likelihood estimator. The von Mises distribution fits very well with the histograms in the first and second plots which is similar to Gaussian except that it is periodic with a period of 2π. We can conclude that the von Mises fits very well with the relative phase pdfs which are in Gaussian shapes.

In Figs. 8(c) and (d), the marginal distributions of the relative phase in these subbands are in peaky and heavy tailed shapes. Evidently, the von Mises distribution is not accurate enough to model these peaky, heavy-tailed pdfs of relative phase. In the next subsection, the wrapped Cauchy distribution is proposed to deal with this type of data.

4.2.2. Wrapped Cauchy distribution

The wrapped Cauchy distribution is obtained by wrapping the Cauchy distribution on the real line with density $f(x)$ around the circle, where

$$f(x)=\frac{\sigma}{\pi(\sigma^2+(x-\mu)^2)},\quad -\infty<x<\infty. \tag{13}$$

It has the probability density function [40,41]

$$p(\theta)=\frac{1}{2\pi}\frac{1-\rho^2}{1+\rho^2-2\rho\cos(\theta-\mu)},\quad -\pi\le\theta\le\pi, \tag{14}$$

where $\rho=e^{-\sigma}$. The wrapped Cauchy density functions in (12) with various values of ρ and μ are shown in Fig. 7.

The wrapped Cauchy distribution is also unimodal and symmetric with the location parameter $-\pi\le\mu\le\pi$ and the scale parameter $0\le\rho<1$. As $\rho\to0$, it tends to the uniform distribution and as $\rho\to1$ it is concentrated at the point $\theta=\mu_0$. The maximum likelihood estimation for this model can be obtained by a recursive algorithm (see Appendix B).

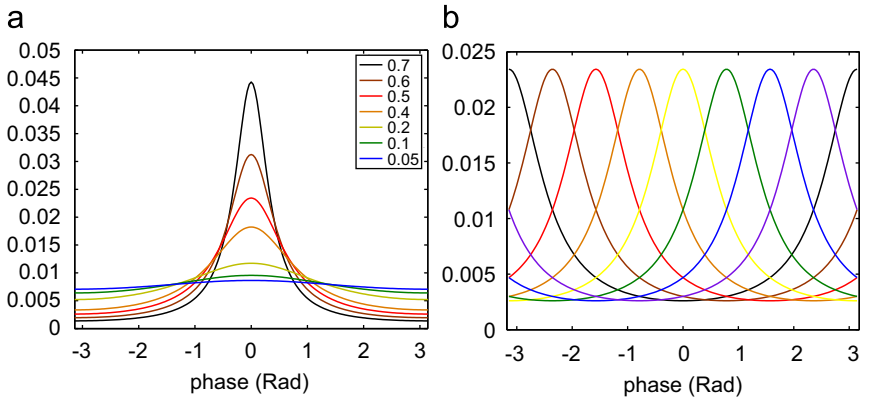

Fig. 7. Wrapped Cauchy distributions: (a) $\rho = [0.05, 0.1, \ldots, 0.7]$ and $\mu = 0$, (b) $\rho = 0.5$ and $\mu = [-\pi, -3\pi/4, \ldots, 3\pi/4]$.

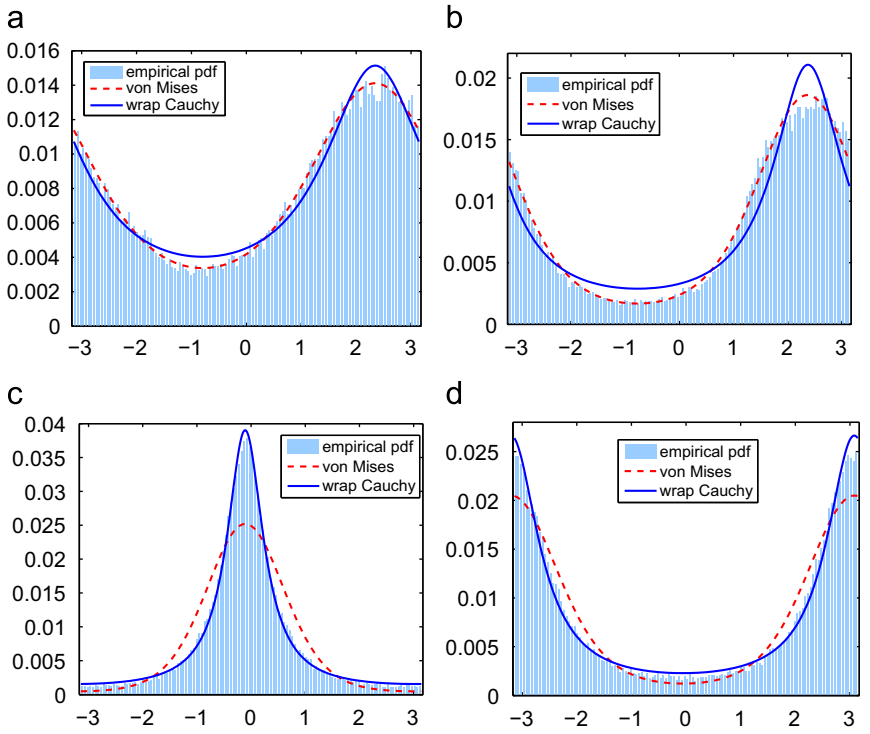

Fig. 8. The von Mises and the wrapped Cauchy distribution fitted to the empirical histograms of relative phase at a particular finest complex wavelet subband. Below each plot are the estimated parameter values, and the relative entropy ΔH (Kullback–Leibler divergence—KLD) between the histogram and the model, as a fraction of the histogram entropy H (with 128 bins).

Fig. 8 shows that the wrapped Cauchy distribution does not fits very well with the histograms in the first and the second plots as the von Mises (Figs. 8(a) and (b)) because the pdfs of the relative phase in these subbands are in Gaussian shapes. However, it fits very well with the histograms in Figs. 8(c) and (d) because the pdfs of relative phase in these subbands are peaky and heavy tailed. Hence, we propose the wrapped Cauchy to model for relative phase pdfs which are in peaky and heavy-tailed shapes and Von Mises for relative phase pdfs which are in Gaussian shapes.

4.2.3. *Comparison of results*

This section details a comparison of the von Mises with the wrapped Cauchy distributions for relative phases in different complex wavelet transforms. We evaluate the von Mises and the wrapped Cauchy for many real images including texture images as well as standard images, which are decomposed by various complex wavelet transforms such as the DTCWT [35], the PDTDFB [19] and the UDCT [20]. The data for evaluation and their information such as the number of subbands, the size of subband and the number of bins are shown in Table 1.

Table 1
Average relative entropy of model and histogram, as a fraction of the total entropy of the histogram ($\Delta H/H$) for von Mises (VM) and wrapped Cauchy (WC) in various complex wavelet domains.

Texture	Subbands	Size	Bins	DTCWT		PDTDFB		UDCT	
				VM	WC	VM	WC	VM	WC
640	3840	64 × 64	32	0.0042	**0.0027**	0.0139	**0.0065**	0.0103	**0.0045**
40	240	128 × 128	64	0.0028	**0.0015**	0.0110	**0.0042**	0.0078	**0.0031**
40	240	256 × 256	128	0.0020	**0.0010**	0.0086	**0.0029**	0.0060	**0.0024**
Lena	6	256 × 256	128	**0.0006**	0.0011	0.0024	**0.0022**	**0.0015**	**0.0015**
Barbara	6	256 × 256	128	**0.0013**	0.0017	**0.0026**	0.0042	**0.0023**	0.0047
Boat	6	256 × 256	128	**0.0020**	0.0025	0.0044	**0.0031**	0.0041	**0.0019**
Fingerp	6	256 × 256	128	0.0014	**0.0007**	0.0098	**0.0029**	0.0092	**0.0029**
Peppers	6	128 × 128	64	**0.0013**	0.0020	0.0045	**0.0028**	0.0029	**0.0023**
House	6	128 × 128	64	0.0024	**0.0018**	**0.0043**	0.0073	**0.0019**	0.0052
Cameram	6	128 × 128	64	**0.0019**	0.0022	0.0033	**0.0025**	0.0043	**0.0027**
Average	4362			0.0020	**0.0017**	0.0065	**0.0040**	0.0050	**0.0031**

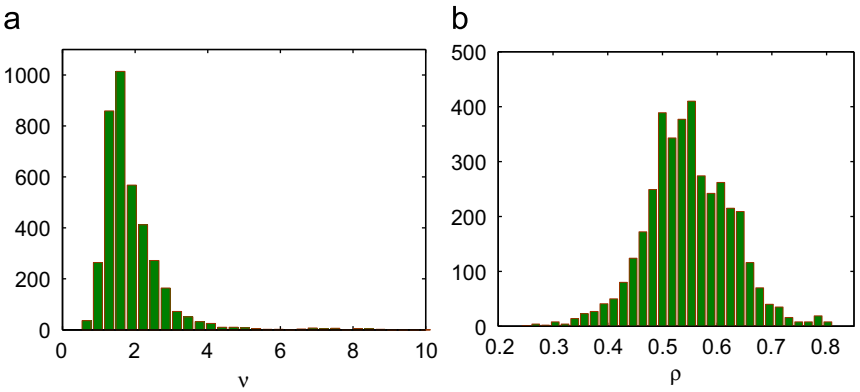

Fig. 9. Histogram of estimated values for the parameter ν (von Mises) and ρ (wrapped Cauchy) of 3840 finest subbands of size 64 × 64 from 640 texture images of size 128 × 128.

The simulation results in Table 1 show that for most of the test images, the wrapped Cauchy model is more accurate than the von Mises. For several images, the accuracy of the fitted wrapped Cauchy model is slightly lower than or approximates that of the von Mises. For all of the above complex wavelet transforms, if compared with the von Mises, the wrapped Cauchy is much better in fitting the relative phase pdf for all texture images and the fingerprint image. The last row in Table 1 presents the average $\Delta H/H$ of all test images. ΔH denotes the Kullback–Leibler divergence (KLD) between the histogram and the model (see Section 5.4.3) and H denotes the histogram entropy. It is clear that compared with von Mises, the wrapped Cauchy is much better in fitting model for relative phases of complex wavelet coefficients.

4.2.4. Range of estimated parameters

It is of interest to know the common range for the values of ν in the von Mises model for texture images as well as of ρ in the wrapped Cauchy model. Fig. 9 shows the histograms of the estimated parameters for 3840 finest subbands of size 64 × 64 from 640 texture images of size 128 × 128 described in Section 5.1. The UDCT is used to decompose texture images. For the von Mises model, most of the values of the estimated ν parameter are from around 1 to 3, while the ρ values of the wrapped Cauchy model are from 0.45 to 0.65.

5. Application in texture image retrieval

The rapid growth in digital electronic technologies, e.g. digital cameras, camcorders and mobile phones as well as the expansion and globalization of networking facilities are enabling a wider use of images, video, diagrams and other visual means to record information and knowledge, while boosting the content growth in digital libraries. Therefore useful multimedia-based search engines for efficient browsing and retrieval of visual information become very necessary. The content-based image retrieval system analyzing the actual contents of the image such as colors, shapes, textures, or any other information that can be derived from the image itself also becomes a subject of interest in image communication.

In this section, a new feature extraction method is proposed for texture image retrieval. The approach based on incorporating the phase information obtained from a

complex wavelet transform. A complex wavelet transform is used to decompose a texture image in order to provide complex subband coefficients. The relative phase statistics, extracted from the phases of the coefficients, is defined as additional features for classification. Performance of the proposed method is compared with the traditional methods. In order to illustrate the improvement of the relative phase-based feature in any complex wavelet transform, we use three multiresolution directional complex wavelet transforms including the DTCWT [35], PDTDFB [19] and UDCT [20]. These complex transforms are similar to each other in terms of directionality of the filters and one-sided supports in the frequency domain. A comparison of various features such as energy feature [42,43], GGD-based feature [44], WD-HMM based feature [45] and our proposed feature in texture retrieval is also presented.

Fig. 10. Two sub-images with the size of 128×128 from the VisTex databases.

5.1. Texture image database and feature database

In our experiment, the texture database contains 40 texture images from the VisTex databases used in [43–45]. Each of these 512×512 images is divided into sixteen 128×128 non-overlapping sub-images, thus creating a database of 640 texture samples. Each original image is treated as a single class and therefore there are 16 samples from each of 40 classes. To reduce the intensity correlation, all images are normalized to have zero mean and unit variance. After that, three decompositions are applied for each image in the database, and their corresponding feature vectors are computed.

5.2. New texture image feature using statistics of relative phase

In this image retrieval application, we propose using statistics of relative phase to extract feature for texture images. When compared with the von Mises, the wrapped Cauchy is much better in fitting the relative phase pdf for all 640 sub-images from VisTex data in Table 1. Therefore, two parameters of the wrapped Cauchy model for relative phase pdfs in each subband will be estimated.

Some examples of both images and their extracted features plus their distributions is illustrated. Two sample sub-images, the Leaves.0011 and the Bark.0000, are from VisTex database as in Fig. 10. Their extracted features, which are the parameters μ and ρ of wrapped Cauchy distributions (Fig. 11), are shown in Table 2. With the same subband, two images have two different relative phase pdfs with different parameters, e.g. at subband 4, the

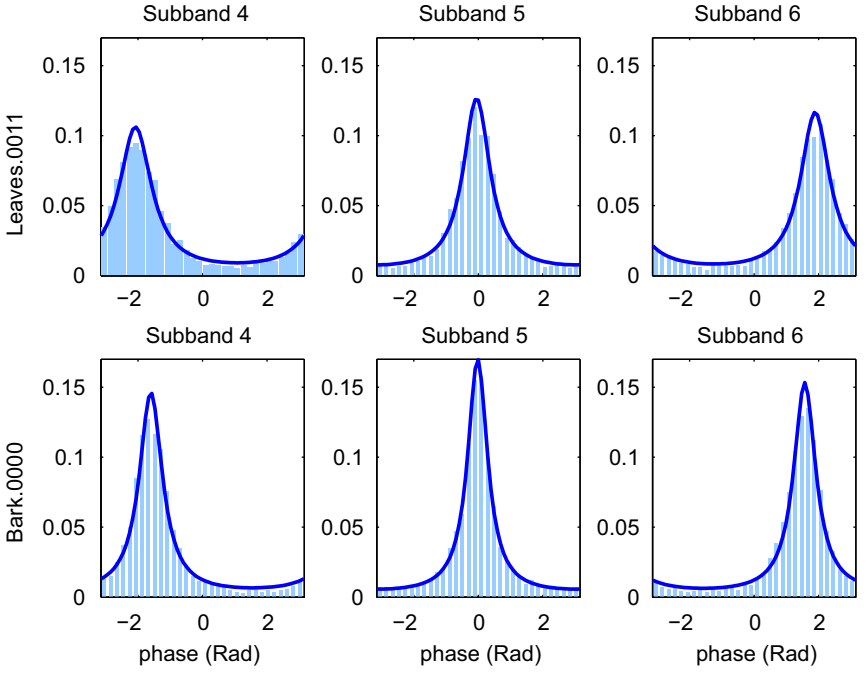

Fig. 11. The wrapped Cauchy distributions fitted to three empirical histograms of relative phase at three subbands 4, 5 and 6 with the size of 64×64 from two sub-images shown in Fig. 10.

Leaves.0011 has the center at $\mu_4 = -2.08$, while the Bark.0000 has the center at $\mu_4 = -1.60$. The relative phase pdf of the Bark.0000 is more peaky with the peak of 0.15 than that of the Leaves.0011 with the peak of 0.10 at subband 4. It is clear that the distinction between two different types of textures can be captured and recognized by the relative phase pdf.

The proposed feature provides statistical information of relative phase for each subband and can be used to discriminate two textures. Therefore, the wrapped Cauchy model of relative phase pdf will be used as an additional feature for texture image retrieval in this section.

Table 2
Some examples of the proposed features using statistics of relative phase (wrapped Cauchy parameters μ and ρ) shown in Fig. 11.

Image	μ_4	μ_5	μ_6	ρ_4	ρ_5	ρ_6
Leaves.0011	−2.08	−0.05	1.89	0.55	0.61	0.58
Bark.0000	−1.60	−0.02	1.57	0.65	0.69	0.66

5.3. Texture feature extraction

Each image in the database is applied to three following decompositions: the DTCWT, the PDTDFB and the UDCT. The DTCWT and the UDCT are applied with four scales and six orientations per scale, while the other has three scales of eight orientations. The mean and standard deviation of the absolute values of the coefficients are calculated as in [42,43]. These features are denoted as magnitude (MAG).

In the traditional energy-based approach, only magnitude of complex coefficients are used to creature feature vector. In this paper, we create a new feature based magnitude as well as phase which we name MAG-RP.

Table 3
Average retrieval accuracy of 40 texture images in the VisTex database using various complex wavelet transforms with features extracted from the finest scale.

N	MAG	MAG-RP	Improve	GGD	GGD-VM	Improve	GGD-WC	Improve
Dual-tree complex wavelet transform								
1	89.38	96.25	7.69	92.34	96.41	4.40	96.56	4.57
3	84.69	93.07	9.90	88.96	93.28	4.86	94.53	6.26
5	80.66	89.47	10.93	85.19	89.75	5.36	90.91	6.71
7	77.30	86.36	11.72	81.58	86.96	6.59	87.99	7.85
10	71.92	81.61	13.47	76.89	82.30	7.03	83.69	8.84
15	63.12	72.71	15.18	67.72	72.16	6.55	73.60	8.69
20	69.04	77.96	12.91	73.52	77.64	5.60	78.97	7.41
30	75.70	83.68	10.54	80.68	83.45	3.43	84.30	4.49
40	80.35	86.82	8.05	84.78	87.06	2.69	88.04	3.85
50	83.83	89.11	6.30	88.20	89.92	1.95	90.68	2.81
60	86.39	90.74	5.04	90.67	92.15	1.63	92.54	2.07
			5.04%			**1.63%**		**2.01%**
			→15.18%			**→7.03%**		**→8.88%**
Pyramidal dual-tree directional filter bank								
1	89.06	94.69	6.32	90.31	96.41	6.75	95.47	5.71
3	85.00	92.66	9.01	87.50	94.11	7.56	94.64	8.15
5	80.88	90.50	11.90	83.38	91.94	10.27	91.81	10.12
7	76.61	87.68	14.45	79.93	89.49	11.95	89.84	12.40
10	71.39	83.84	17.44	74.33	85.53	15.07	85.58	15.14
15	62.80	75.74	20.60	65.47	76.66	17.09	77.35	18.15
20	68.21	81.16	18.98	70.94	81.80	15.32	82.39	16.14
30	74.84	86.34	15.37	77.57	87.17	12.37	87.06	12.23
40	79.22	89.33	12.77	82.00	90.49	10.35	89.97	9.72
50	82.44	91.48	10.97	85.38	92.64	8.50	92.41	8.24
60	84.95	92.95	9.42	87.64	94.10	7.38	93.94	7.19
			6.32%			**6.75%**		**5.71%**
			→20.60%			**→17.09%**		**→18.15%**
Uniform discrete curvelet transform								
1	86.72	95.63	10.27	87.81	96.72	10.14	96.72	10.14
3	82.60	94.32	14.19	85.73	95.31	11.18	94.95	10.75
5	78.78	91.56	16.22	81.91	93.13	13.70	92.91	13.43
7	75.07	89.33	19.00	78.24	90.78	16.03	90.29	15.41
10	70.27	85.31	21.41	73.45	86.89	18.29	86.38	17.59
15	62.20	76.95	23.71	64.60	78.86	22.07	78.41	21.36
20	67.98	81.95	20.55	70.86	83.40	17.68	82.91	16.99
30	74.55	86.00	15.36	78.14	87.66	12.19	87.39	11.84
40	79.02	88.52	12.02	82.97	90.39	8.94	90.02	8.50
50	82.64	90.45	9.45	85.89	92.13	7.27	91.68	6.74
60	85.35	91.82	7.58	88.10	93.40	6.01	93.00	5.56
			7.58%			**6.01%**		**5.56%**
			→23.71%			**→22.07%**		**→21.36%**

Table 4
Average retrieval rates over the whole database for various methods when $N = 15$.

Methods	Feature length	Rate (%)
Standard DWT: L1 + L2	18	64.83
GGD [44]	18	75.73
Scalar WD-HMM [45]	33	76.51
Vector WD-HMM [45]	41	80.05
DT-CWT + DT-RCWT [43]	80	81.16
Proposed method: GGD-WC	48	**85.64**

First, the relative phase matrix of each complex subband in the complex wavelet domain are computed as in (5), and circular mean and standard deviation of this relative phase matrix will be estimated by (9) and (11) to form the relative phase feature. After that, we combine the MAG feature and the relative phase feature to create the MAG-RP feature.

In the statistical approach, two parameters of the GGD model for real coefficients in each subband will be estimated by [44]. In our new approach, we will create a feature based on a real part model as well as a imaginary part model using the GGD and relative phase models, which we name GGD-VM and GGD-WC. For each relative phase matrix, two parameters μ and v of the von Mises model are estimated using maximum-likelihood as shown in Appendix A, and two parameters μ and ρ of the wrapped Cauchy model are also estimated by the maximum likelihood estimator obtained by a recursive algorithm as in Appendix B. These parameters are used to form the von Mises and wrapped Cauchy feature vectors.

In the first experiment with results shown in Table 3, we only use all subbands at the finest scale. The DTCWT and the UDCT have six subbands. Each subband is extracted by two parameters. Therefore, the length of MAG or GGD feature is $6 \times 2 = 12$, and the length of relative phase, von Mises and wrapped Cauchy feature is also 12. The combination of these feature will create the length double.

In the second experiment with results shown in Table 4, we use the UDCT and create the feature vector with length 48. This proposed feature contains 24 GGD parameters of two finest scales, 12 wrapped Cauchy parameters of the finest scale, and 12 MAG means of two coarsest scales. Since the size of sub-image is 64, the relative phase models are only accurate enough for subbands at the finest scale with the size of 32. Therefore, the relative phase models of the finest scale should be used to form feature vector for retrieval application. Similarly, the GGD models of two finest scales will be estimated. The feature of remaining subbands from two coarsest scales will be extracted by computing the mean of absolute values.

5.4. Distance measure and query processing

5.4.1. Distance measure between two MAG features

The query pattern can be any one of the texture patterns from the image databases. Let f_x and f_y be two MAG feature vectors obtained from one of the three transforms. The distance between them is given by [42]

$$d = \sum_k \left(\left| \frac{m_k(x) - m_k(y)}{\alpha(m_k)} \right| + \left| \frac{\sigma_k(x) - \sigma_k(y)}{\alpha(\sigma_k)} \right| \right), \tag{15}$$

where $\alpha(m_k)$ and $\alpha(\sigma_k)$ are the standard deviations of $m_k(\cdot)$ and $\sigma_k(\cdot)$ of the entire database.

5.4.2. Distance measure between two relative phase features

Let f_x and f_y be two relative phase feature vectors. We propose the distance between them as follows:

$$d = \sum_k \left| \frac{S_k(x) - S_k(y)}{\alpha(S_k)} \right| + \frac{1 - \cos(\overline{\theta}_k(x) - \overline{\theta}_k(y))}{\alpha(\overline{\theta}_k)},$$

where $\alpha(S_k)$ is the standard deviations of $S_k(\cdot)$ and $\alpha(\overline{\theta}_k)$ is the circular variance of $\overline{\theta}_k(\cdot)$ of the entire database.

Since circular mean $\overline{\theta}$ is circular data, we will need a discrimination rule based on a circular distance. For any two points on the unit circle (θ_i, θ_j), the circular distance is defined by $d_{ij} = 1 - \cos(\theta_i - \theta_j)$. It is non-negative, symmetric in its indices and is invariant under rotation. To normalize the circular mean features over the whole database, instead of using d_{ij} divided by the standard deviation as in [42], we replace the standard deviation by the circular variance of $\overline{\theta}_k(\cdot)$ of the entire database. Another feature of relative phase is circular variance S which is not circular data, we will compute the L_1 distance divided by the standard deviation of $S_k(\cdot)$ of the entire database.

5.4.3. Similarity measurement between two models

Given the von Mises model, the relative phase pdf in each subband can be defined via two parameters μ and v. The Kullback–Leibler divergence (KLD) or the relative entropy between two pdfs $p(\theta; \mu_1, v_1)$ and $p(\theta; \mu_2, v_2)$ is

$$D_{KL}(P\|Q) = \int_{-\pi}^{\pi} p(\theta; \mu_1, v_1) \log \frac{p(\theta; \mu_1, v_1)}{p(\theta; \mu_2, v_2)} \, d\theta. \tag{16}$$

Substitute (12) into (16) and after some manipulations we obtained a closed form for the KLD between two VMs as

$$D_{KL} = \log \frac{I_0(v_2)}{I_0(v_1)} + \frac{I_1(v_1) - I_1(-v_1)}{2I_0(v_1)}(v_1 - v_2 \cos(\mu_2 - \mu_1)), \tag{17}$$

where I_1 denotes the modified Bessel function of the first kind and order one which can be defined by $I_1(v) = (1/\pi) \int_0^{\pi} e^{v\cos\theta} \cos\theta \, d\theta$. Therefore, the similarity measurement between two complex wavelet subbands can be calculated very efficiently using the model parameters. The overall similarity distance between two images is the sum of the KLDs given in (17) between corresponding pairs of all wavelet subbands as follows:

$$d = \sum_k D_{KL}(p(.; \mu_k(x), v_k(x)) \| p(.; \mu_k(y), v_k(y))). \tag{18}$$

Instead of using the von Mises model, we can use the wrapped Cauchy for modeling the RPs in each subband via two parameters μ and ρ. The Kullback–Leibler divergence (KLD) between two pdfs $p(\theta; \mu_1, \rho_1)$ and $p(\theta; \mu_2, \rho_2)$ is also given by (16), where von Mises density is replaced by

wrapped Cauchy density and the overall similarity distance between two images is similar to (18). However, a closed form for the KLD between two WCs is under investigation, and a numerical method with 128 bins is applied to estimate this KLD.

5.4.4. Query processing

For each query image, N nearest neighbors are selected, and the number of these textures belonging to the same class as the query texture, except for itself, is counted. This number (less than or equal to 15) divided by 15 if $N>15$ and divided by N if $N<15$ is defined as the retrieval rate. The performance of the entire class is obtained by averaging this rate over 16 members which belong to the same class of texture. The average of all classes is the overall performance of the transform.

5.5. Experimental results

In the first experiment, the average retrieval rates of new approach based on both magnitude and phase can significantly improve up to 8.69–23.71% when the top 15 texture images that are nearest to the search texture are considered ($N=15$) as shown in Table 3. Table 3 summarizes the overall retrieval rates when we use only all subbands from the finest scale of three different complex directional wavelet transforms. The parameters of different feature vectors are detailed in Table 5. The MAG-RP is consistently better than the MAG, and the GGD-WM and GGD-WC are consistently better than the GGD as shown in Table 3. We observe that when using phase the retrieval rates are significantly higher than without using phase. The improvement occurs at any N from 1 to 60 and this agrees with all of three complex wavelet transforms. The DTCWT yields the improvement rate of 2.01–15.18%, while the PDTDFB gains 5.71–20.60% and the UDCT gains 5.56–23.71%. It is clear that this improvement is caused by the presence of the relative phase in the new feature vector. The relative phase information in the proposed approach can definitely support the existing methods including energy-based method as well as the GGD-based method.

When number of texture images selected N increases with ($N<15$), the performance decreases but the improvement rate will increase. On the contrary for the cases of $N>15$, the performance increases but the improvement rate will decrease. Therefore the improvement rate will be maximum at $N=15$ in most cases.

In the second experiment with the same database, 40 VisTex textures, the performance of our proposed method is compared with the performances of different existing methods including energy based feature [43], GGD-based feature [44], WD-HMM based feature [45]. Simulation results in Table 4 show that our proposed method outperforms the others. The feature vectors of all previous methods are extracted from the magnitudes or the real values of wavelet subbands, while our method exploits the phase of complex coefficients and extracts image information in both magnitude and phase. The incorporated phase information which is absolutely complementary to magnitude is the reason why the new feature can achieve better performance than the others.

5.6. Computational complexity and time

The proposed texture retrieval method is implemented in MATLAB R2006a. With an Intel core 2 CPU 2.13 GHz machine, the feature vector time and the similarity measurement time of different features are shown in Table 5.

The time to extract the proposed feature GGD-WC with the length of 48 from one image is about 0.667 second (s). It includes 0.039 s for decomposing image using the UDCT (four scales and six subbands each scale), 0.259 s for estimating 24 GGD parameters of two finest scales, 0.003 s for computing 12 MAG features of two coarsest scales and 0.366 s for estimating 12 wrapped Cauchy parameters of the finest scales. It take more time to extract the GGD-WC feature vector than the other features as shown in Table 5. This can be a weak aspect of the proposed method. However, the time to extract a feature vector from one image is still much less than 1 s. Therefore, this proposed feature can be suitable for real-time applications.

With the same feature vector length, the similarity measurement time between two images using the GGD-VM which is 0.769 ms is much less than 2.245 ms when using the GGD-WC. The reason is that we derived the closed form of distance between two von Mises as in (17) while a closed form for the KLD between the two wrapped Cauchy pdfs is developing and we have to use a numerical method with 128 bins to estimate this KLD. Therefore, instead of using the wrapped Cauchy, we can use von Mises for a fast feature extraction and searching time. Although the wrapped Cauchy is better than von Mises in fitting model for relative phase of complex wavelet coefficients, the performance of the von Mises feature is still comparable with the performance of the wrapped Cauchy feature in texture image retrieval application as shown in Table 3.

In this experiment, with the database of 640 images, it takes about 1.5 s to retrieve 15 images which are similar to the query image. This searching time is still acceptable.

Table 5
Feature vector length, feature extraction time and similarity measurement time of query image.

	MAG	MAG-RP	GGD	GGD-VM	GGD-WC	GGD-WC
Feature vector type	m,σ	m,σ,$\overline{\theta}$, S	α,β	α,β,μ,ν	α,β,μ,ρ	α,β,μ,ν,m
Feature vector length	12	24	12	24	24	48
Feature extraction time (s)	0.076	0.118	0.262	0.291	0.628	0.667
Similarity measurement time (between two images) (ms)	0.058	0.562	0.198	0.769	2.245	2.314

However, if the database is huge, the numerical method for estimating KLD between the two wrapped Cauchy is a disadvantage of the searching time of the proposed method. The fast estimation algorithm for KLD between the two wrapped Cauchy is the future work.

6. Application in texture segmentation

Texture segmentation is an important application for image analysis. It has been studied intensively and many different feature extraction schemes have been proposed. One of the common approach in texture segmentation is to use a filter bank to decompose a texture image into subbands [46,47]. The Gabor filters are widely used in feature extraction for texture segmentation [48–50]. Textures are also characterized by features extracted from images modeled in multiresolution domain as Markov random field [51], hidden Markov tree [52] and coupled Markov random field [53]. Some other works characterize texture by its rotation invariant roughness using fractal dimension [54], adaptive scale fixing [55] and local spectral histogram [56]. How magnitude and phase information of the complex wavelet coefficients can be used to segment texture images will be discussed in this section.

6.1. Local mean direction feature for texture segmentation

Since relative phases can represent a dominant direction within a directional subband, it is used in the texture image retrieval as shown in Section 5. Note that the relative phase feature proposed for image retrieval determines the global mean direction of the dominant orientations in the whole subband and the circular variance determines the measure of global dispersion for these dominant orientations. Since this feature vector represents the global information, we are not able to use it to discriminate the pixels in segmentation problems. In this section, we discuss how to develop the magnitude and phase based feature extraction method to make it suitable for texture segmentation.

Suppose that there is an edge of angle α_k at position (i,j). From (2) and (4) this angle can be estimated from the relative phase $\theta_{sk}(i,j)$ by

$$\alpha_k \approx \gamma_k - \tan\gamma_k + \frac{\theta_{sk}(i,j)}{a_{sk}D_s\cos\gamma_k}, \tag{19}$$

where γ_k is the center angle of the subband, and a_{sk} is a constant estimated in the neighborhood of (i,j). In our segmentation algorithm, the relative phase $\theta(i,j)$ is replaced by the local mean direction (LMD) of the relative phases in the local window W, i.e.

$$\alpha_k \approx \gamma_k - \tan\gamma_k + \frac{\hat{\theta}_{sk}(i,j)}{a_{sk}D_s\cos\gamma_k}, \tag{20}$$

where $\hat{\theta}_{sk}(i,j)$ is the LMD at (i,j) which is defined by

$$\hat{\theta}_{sk}(i,j) = \arctan\frac{\sum_{i,j\in W}\sin\theta(i,j)}{\sum_{i,j\in W}\cos\theta(i,j)}. \tag{21}$$

The LMD is also computed by (21) for all other values of k. We can see that the angle of the edge can be estimated from the relative phase $\theta_{sk}(i,j)$ in the neighbor of an edge. Hence the relative phase $\theta_{sk}(i,j)$ is approximately constant in the vicinity of an edge, and when evaluated in directional subbands, the LMDs can be used to identify the edge direction. The quality of texture segmentation depends on the window size. When a large window is used, a sufficient amount of information is captured. However, a small window is necessary to accurately locate the boundaries between texture regions. This suggests that the selection of window size could possibly be based on the contents of the image. The images with larger texture would require larger window sizes, whereas finer textures would require smaller windows. In our experiments, the 5×5 window is used for the texture images and the 3×3 window is used for the real images.

Fig. 12 illustrates the difference between the phase and the LMD. Each image is a combination between two different types of textures (D17 and D55). In Figs. 12(a) and (c), each arrow represents the magnitude (length) and phase (angle) of the PDTDFB coefficient, while in Figs. 12(b) and (d), the angle represents the estimated angle calculated from the LMDs above. It is clear that the distinction of the LMDs between the two types of textures D17 and D55 can be captured and recognized in Figs. 12(b) and (d) while no clear distinction is obtained from the phase of PDTDFB coefficients. Since the LMD determines the local mean direction of the dominant orientations θ_k in the small window, it provides local information of the subband images and can discriminate the pixels. Therefore, the LMD will be used as an additional feature for texture segmentation.

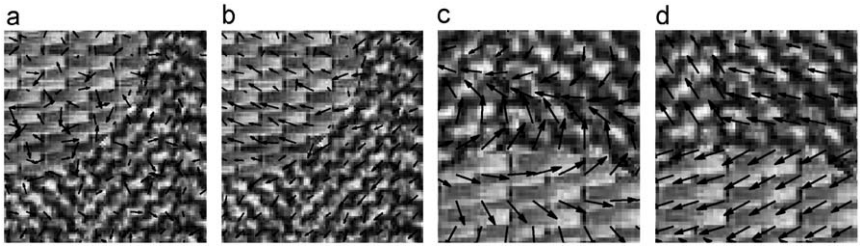

Fig. 12. D17D55 image cropped. (a) PDTDFB phase ($s=2$, $k=2$), (b) PDTDFB–LMD ($s=2$, $k=2$), (c) PDTDFB phase ($s=5$, $k=3$), and (d) PDTDFB–LMD ($s=5$, $k=3$).

6.2. Proposed segmentation method

The framework of the proposed method is shown in Fig. 13. A texture image is first decomposed by the PDTDFB. The complex-valued subband images obtained from the PDTDFB are then used to extract local magnitude and phase features. For magnitude, a local smoothing window of size $M \times M$ is applied to the magnitude of complex coefficients. Therefore, each pixel of the output of window represents an average magnitude of the $M \times M$ block. For phase, a local mean direction at a pixel is determined by the phases of complex coefficients in the local $M \times M$ block.

The classification is tested on two groups of synthetic texture images from the Brodatz album [57] in our experiments. The texture images used in the first experiment contains 15 images, each composing of two different types of textures. The second group of textures consists of five images where each has five types of textures. The size of these images is 256×256. For each experiment, each image in the database is decomposed by the following three decomposition methods: the 2-D Gabor transform, the DTCWT and the PDTDFB. The numbers of scales and orientations are chosen to give the best results. The Gabor transform is applied with six scales and eight orientations per scale while the DTCWT has six scales of six orientations (recall that the number of orientations of the DTCWT is fixed to six), and the PDTDFB has five or six scales of eight orientations.

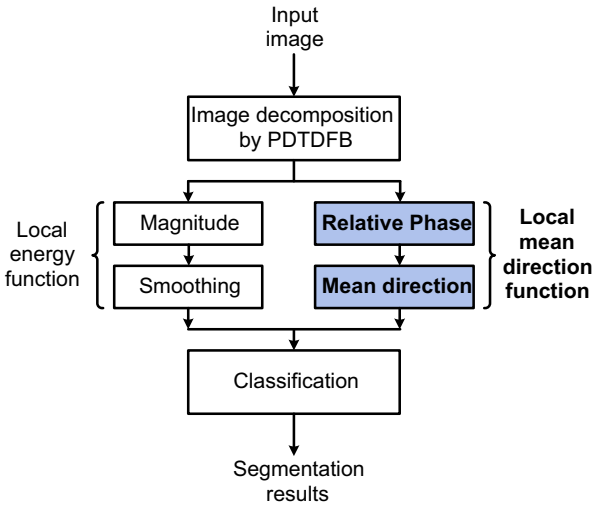

Fig. 13. The block diagram for the PDTDFB–LMD-based segmentation of texture images.

The local energy is computed over a window by

$$e_k(i,j) = \frac{1}{N} \sum_{(m,n) \in W} w_{mn} |y_k(i-m, j-n)|, \quad (22)$$

where N is the number of elements in the window W. In our experiments, the running average window is used although any other type of windows such as the Gaussian weighted window can also be applied [49]. In texture segmentation, neighboring pixels are very likely to belong to the same texture category. We include the spatial coordinates of the pixel as additional features as proposed in [49] for the five-texture image segmentation. For the case of two-texture image segmentation, the spatial

Table 7
Comparison of different feature extraction schemes in segmentation of five-texture images.

	Gabor	PDTDFB	PDTDFB-LMD
# scales	6	6	6
# orientations	8	8	8
# features	50	50	98
Ave. errors (%)	4.4	4.7	2.6
Improvement (%)			**46.0**

Table 6
Comparison of different feature extraction schemes in segmentation of two-texture images.

	Gabor/ + LMD	DTCWT/ + LMD	PDTDFB/ + LMD
# scales	6/6	6/6	5/5
# orientations	8/8	6/6	8/8
# features	48/96	36/72	40/80
D21-79	3.3/2.1	2.8/2.4	2.7/1.3
D68-6	2.8/1.3	3.3/2.2	1.6/1.4
D101-106	1.6/1.4	2.1/1.6	3.0/1.6
D12-8	2.3/2.2	2.7/2.1	3.5/2.3
D105-16	1.9/1.2	1.4/1.1	2.8/1.7
D21-57	2.1/1.9	2.1/1.7	2.2/1.4
D103-26	2.6/2.4	2.0/1.3	2.7/2.1
D17-72	2.0/1.8	3.7/4.0	2.8/2.2
D54-56	12.7/5.6	12.9/5.4	7.5/4.8
D21-4	2.5/2.2	2.9/2.3	3.2/1.7
D17-55	1.7/2.2	3.9/2.1	4.2/2.2
D21-77	1.8/1.2	1.6/0.7	1.2/1.0
D73-106	1.1/1.2	0.8/0.9	2.2/2.1
D21-83	3.7/3.1	3.9/2.9	4.2/2.2
D85-11	1.6/1.6	4.7/4.2	3.4/2.5
Ave. error (%)	2.9/2.1	3.4/2.3	3.1/2.0
Improvement after using phase (%)	**27.7**	**31.3**	**35.4**

coordinates are not used because the same performance is obtained when adding these two coordinate features. The LMD features of subbands are estimated by (21).

When using filter banks, the most frequent segmentation method is to search for class prototypes in the feature space by clustering the feature vectors according to certain rules. Each image pixel is classified by determining the class prototype which is closest to its feature vector. In our experiments, we use the standard *K*-means clustering algorithm used in [58]. Before clustering each feature is normalized to have a zero mean and a constant variance. Some other complex classification methods may also be applied to further improve the segmentation results. However, this is beyond the scope of the work and might smear the effect of the LMD feature.

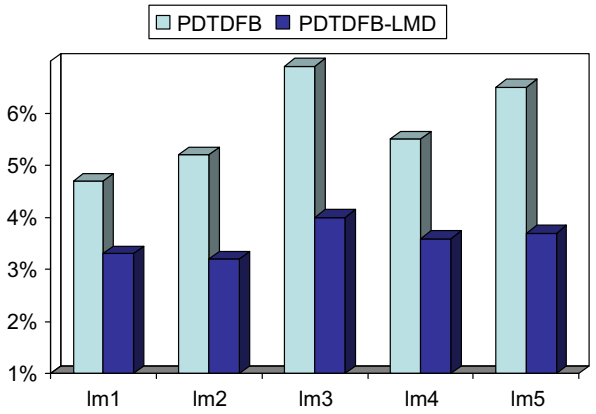

Fig. 14. Percentage errors for PDTDFB and PDTDFB–LMD in segmentation of five-texture images.

6.3. Simulation results

Table 6 summarizes classification error rates using different directional transforms for the 15 two-texture images. The average error rates of the methods using phase are consistently much lower than when using magnitude alone. The combination of PDTDFB and LMD (PDTDFB–LMD) yields the best overall segmentation performance of 2.0%. This corresponds to an improvement of 35.4% from using only magnitude. The improvements after phase incorporation for the cases of the Gabor transform (Gabor–LMD) and the DTCWT (DTCWT–LMD) are 27.7% and 31.3%, respectively.

In the second experiment with five five-texture images, the average classification error rates for the PDTDFB and PDTDFB–LMD are summarized in Table 7. The average error rate for the case of PDTDFB–LMD is 2.6%, much

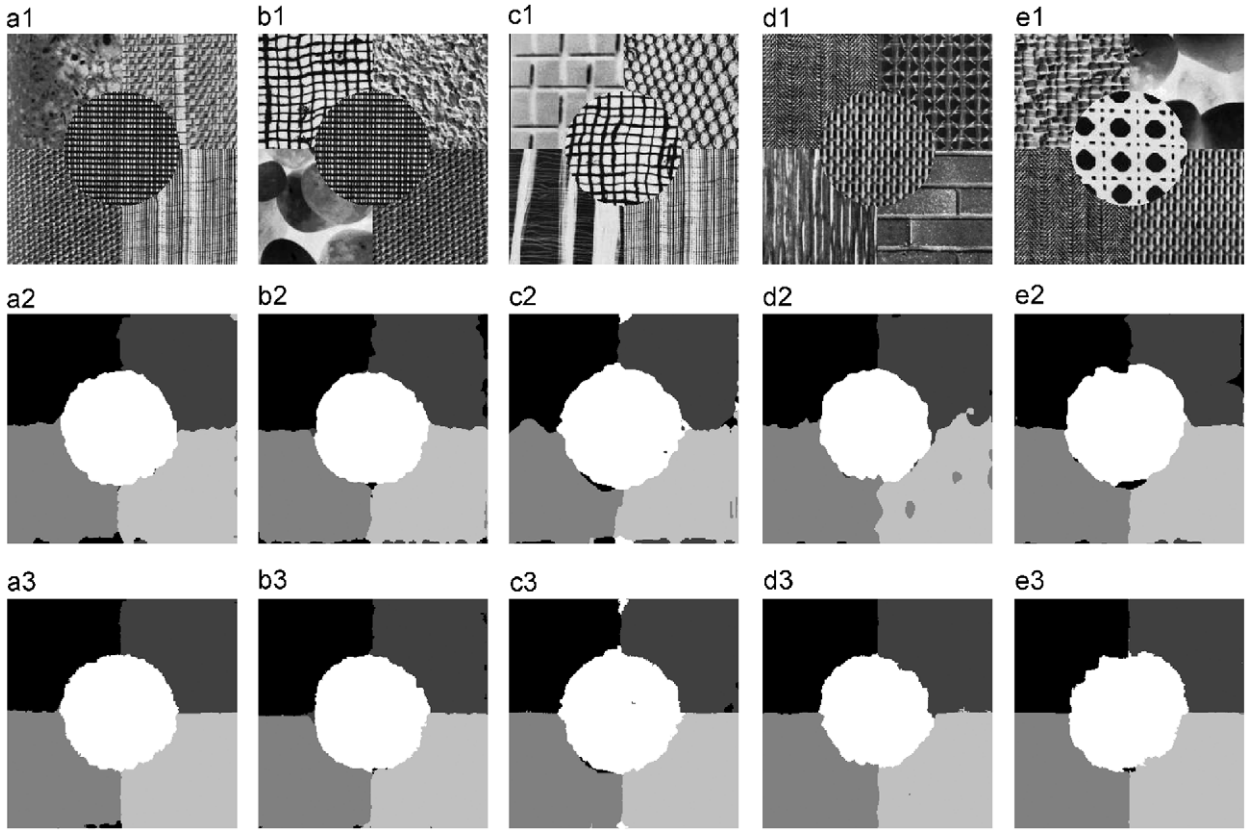

Fig. 15. Segmentation of five-texture images. (a1)–(e1): the 256 × 256 synthetic images from Brodatz album; (a1) Im1 image composed of D73, D85, D77, D106 and D21; (b1) Im2: D104, D4, D30, D77 and D21; (c1) Im3: D1, D36, D51, D106 and D104; (d1) Im4: D16, D52, D68, D94 and D53; (e1) Im5: D84, D30, D16, D53 and D101. (a2)–(e2) segmentation results using PDTDFB. (a3)–(e3) segmentation results using PDTDFB-LMD.

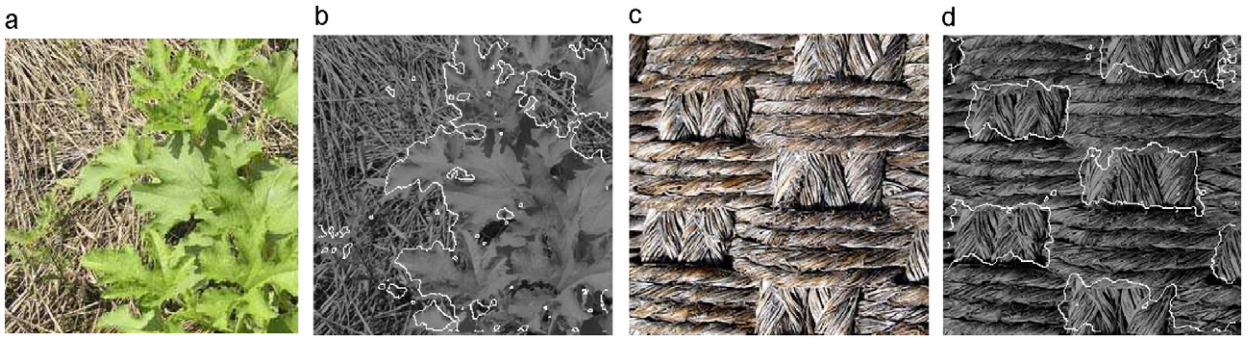

Fig. 16. Segmentation of real images: (a) pumpkinplant image, (c) island texture, (b) and (d) segmentation results using PDTDFB–LMD.

lower than that of the case of PDTDFB which is 4.7%. In this case, the improvement of the PDTDFB–LMD after using phase information is 46%. Fig. 14 shows percentage errors of each of the five five-texture images for the PDTDFB and PDTDFB–LMD. It is evident that the PDTDFB–LMD yields a nice improvement compared to the PDTDFB which is based on magnitude information alone. Using this classification result, the segmentation results for the five images are shown in Fig. 15. It is clear that the phase information can complement to magnitude information because higher classification accuracy and better boundaries are achieved. Fig. 16 shows the segmentation results of some real images. The color images are converted to the gray-scale images before segmentation.

From the simulations, the segmentation results after using phase are much better (27.7–46% improvement) than using magnitude alone in term of classification error rate with different texture images.

7. Conclusion

A new approach which exploits the probabilistic properties from the phase information of 2-D complex wavelet coefficients for the image modeling is studied. The property and statistics of relative phase are investigated. We conclude that the von Mises fits very well only with the relative phase pdfs which are in Gaussian shapes. The wrapped Cauchy is proposed for the relative phase pdf which is in peaky and heavy-tailed shape. The parameters of the von Mises and wrapped Cauchy pdf are estimated by maximum-likelihood estimators. We demonstrate that the wrapped Cauchy captures the peaky and heavy-tailed behaviors of relative phases. The simulation results show that for most of the test images, the wrapped Cauchy model is more accurate than the von Mises, when images are decomposed by different complex wavelet transforms. The statistics of relative phases are then applied to several image processing applications, including texture image retrieval and texture segmentation. Our processing method employed feature extraction scheme in which phase information is incorporated yields a higher retrieval accuracy. The incorporated phase information which is complementary to magnitude is the reason why the new feature can achieve better performance than the others. The proposed relative phase approach can be applied to any complex wavelet transform and can be a promising approach for other applications in image processing.

Appendix A. Maximum likelihood estimation for von Mises distribution

Let $\theta_1, \theta_2, \ldots, \theta_n$ be a set of observations from a von Mises distribution with parameters μ and v, then $\theta_1, \theta_2, \ldots, \theta_n$ are i.i.d with pdf

$$p(\theta;\mu,v) = \frac{1}{2\pi I_0(v)} e^{v\cos(\theta-\mu)}, \quad -\pi \le \theta < \pi. \tag{23}$$

The log likelihood function is given by

$$l = \log L = -n\log(2\pi I_0(v)) + v\sum_{i=1}^{n}\cos(\theta_i - \mu). \tag{24}$$

Differentiating (24) with respect to μ and v, and equating to zero, we obtain the likelihood equations

$$\frac{\partial l}{\partial \mu} = \sum_{i=1}^{n}\sin(\theta_i - \mu) = 0, \tag{25}$$

$$\frac{\partial l}{\partial v} = -nA(v) + \sum_{i=1}^{n}\cos(\theta_i - \mu) = 0, \tag{26}$$

where $A(v) = I_1(v)/I_0(v)$ and $I_1(v) = dI_0(v)/dv$, the modified Bessel function of order 1.

From Eq. (25), we have

$$\hat{\mu} = \arctan\frac{\sum_{i=1}^{n}\sin(\theta_i)}{\sum_{i=1}^{n}\cos(\theta_i)}, \tag{27}$$

where arctan is the four-quadrant inverse tangent.

From Eq. (26), the maximum likelihood estimate $\hat{v}$ of v is the solution of

$$A(v) = \frac{\sum_{i=1}^{n}\cos(\theta_i - \hat{\mu})}{n} = \overline{R}, \tag{28}$$

$$\hat{v} = A^{-1}(\overline{R}). \tag{29}$$

The solution of (29) can only be obtained numerically. The approximate solutions to (29) can be obtained as follows:

$$\hat{v} = \begin{cases} 2\overline{R} + \overline{R}^3 + \frac{5}{6}\overline{R}^5, & 0 \le \overline{R} < 0.53, \\ -0.4 + 1.39\overline{R} + \frac{0.43}{(1-\overline{R})}, & 0.53 \le \overline{R} < 0.85, \\ \frac{1}{(\overline{R}^3 - 4\overline{R}^2 + 3\overline{R})}, & \overline{R} \ge 0.85. \end{cases} \quad (30)$$

Appendix B. Maximum likelihood estimation for wrapped Cauchy distribution

$$\text{Set } \mu_1 = \frac{2\rho\cos\mu}{1+\rho^2}, \quad \mu_2 = \frac{2\rho\sin\mu}{1+\rho^2}, \quad c = \frac{1}{\sqrt{1-\mu_1^2-\mu_2^2}}, \quad (31)$$

$$\eta_1 = c\mu_1, \quad \eta_1 = c\mu_2 \quad \text{and} \quad c = \sqrt{1+\eta_1^2+\eta_2^2}. \quad (32)$$

The wrapped Cauchy distribution becomes

$$p(\theta, \eta_1, \eta_2) = \frac{1}{2\pi(\sqrt{1+\eta_1^2+\eta_2^2}} - \eta_1\cos\theta - \eta_2\sin\theta). \quad (33)$$

Differentiating the log likelihood function with respect to η_1 and η_2 leads to the likelihood equations

$$\frac{1}{c}\sum_{i=1}^{n} w_i(\cos\theta_i - \mu_1) = 0, \quad \frac{1}{c}\sum_{i=1}^{n} w_i(\sin\theta_i - \mu_2) = 0, \quad (34)$$

where $i = 1, 2, \ldots, n$, and

$$w_i = \frac{1}{1 - \mu_1\cos\theta_i - \mu_2\sin\theta_i}. \quad (35)$$

These equations can be written as

$$\mu_1 = \frac{\sum_{i=1}^{n} w_i\cos\theta_i}{\sum_{i=1}^{n} w_i}, \quad \mu_2 = \frac{\sum_{i=1}^{n} w_i\sin\theta_i}{\sum_{i=1}^{n} w_i}. \quad (36)$$

The iterative re-weighting algorithm for maximum likelihood estimator can be given step-by-step as follows.

1. Initialize $\mu_1^{[0]}$ and $\mu_2^{[0]}$ with $\mu_1^{[0]} + \mu_2^{[0]} < 1$, and calculate $w^{[0]}$ using (35).
2. Given $\mu_1^{[k]}$, $\mu_2^{[k]}$ and $w^{[k]}$ at iteration k, calculate $\mu_1^{[k+1]}$ and $\mu_2^{[k+1]}$ using (36).
3. Repeat step 2 until the algorithm converges, giving $\hat{\mu}_1$ and $\hat{\mu}_2$
4. Calculate $\hat{\mu}$ and $\hat{\rho}$ by

$$\hat{\mu} = \arctan\frac{\hat{\mu}_2}{\hat{\mu}_1} \quad \text{and} \quad \hat{\rho} = \frac{1 - \sqrt{1-\hat{\mu}_1^2-\hat{\mu}_2^2}}{\sqrt{\hat{\mu}_1^2+\hat{\mu}_2^2}}. \quad (37)$$

References

[1] S. Mallat, A Wavelet Tour of Signal Processing, Academic Press, San Diego, 1998.

[2] E.P. Simoncelli, Handbook of Video and Image Processing, second ed., Academic Press, New York, 2005, pp. 431–441 (Chapter 4).

[3] P. Moulin, J. Liu, Analysis of multiresolution image denoising schemes using generalized Gaussian and complexity priors, IEEE Transactions on Information Theory 45 (3) (1999) 909–919.

[4] E.P. Simoncelli, Bayesian denoising of visual images in the wavelet domain, in: P. Müller, B. Vidakovic (Eds.), Bayesian Inference in Wavelet Based Models, Springer, New York, 1999, pp. 291–308 (Chapter 18).

[5] H.A. Chipman, E.D. Kolaczyk, R.E. Mcculloch, Adaptive Bayesian wavelet shrinkage, Journal of the American Statistical Association 92 (1997) 1413–1421.

[6] M.S. Course, R.D. Nowak, R.G. Baraniuk, Wavelet-based signal processing using hidden Markov models, IEEE Transactions on Signal Processing 46 (4) (1998) 886–902 (Special issue on Wavelets and filter banks).

[7] J.K. Romberg, H. Choi, R.G. Baraniuk, Bayesian tree-structured image modeling using wavelet-domain hidden Markov models, IEEE Transactions on Image Processing 10 (7) (2001) 1056–1068.

[8] M.J. Wainwright, E.P. Simoncelli, Scale mixtures of Gaussians and the statistics of natural images, Advances in Neural Information Processing Systems 12 (2000) 855–861.

[9] L. Sendur, I.W. Selesnick, Bivariate shrinkage functions for wavelet-based denoising exploiting interscale dependency, IEEE Transactions on Signal Processing 50 (11) (2002) 2744–2756.

[10] S. LoPresto, K. Ramchandran, M.T. Orchard, Wavelet image coding based on mixture modeling of wavelet coefficients and a fast estimation-quantization framework, in: Proceedings of the Conference on Data Compression, 1997, pp. 221–230.

[11] K. Mihçak, I. Kozintev, K. Ramchandran, P. Moulin, Low-complexity image denoising based on statistical modeling of wavelet coefficients, IEEE Signal Processing Letters 6 (12) (1999) 300–303.

[12] J. Portilla, E.P. Simoncelli, A parametric texture model based on joint statistics of complex wavelet coefficients, International Journal of Computer Vision 40 (1) (2000) 49–71.

[13] J. Portilla, V. Strela, M.J. Wainwright, E.P. Simoncelli, Image denoising using scale mixtures of Gaussians in the wavelet domain, IEEE Transactions on Image Processing 12 (11) (2003) 1338–1351.

[14] H. Choi, J.K. Romberg, R.G. Baraniuk, N. Kingbury, Hidden Markov tree modeling of complex wavelet transforms, in: Proceedings of IEEE International Conference on Acoustics, Speech, and Signal Processing (ICASSP'00), vol. 1, 2000, pp. 133–136.

[15] J.K. Romberg, H. Choi, R.G. Baraniuk, N. Kingbury, Multiscale classification using complex wavelets and hidden Markov tree models, in: Proceedings of IEEE International Conference on Image Processing (ICIP'00), vol. 2, 2000, pp. 371–374.

[16] C.W. Shaffrey, N.G. Kingsbury, I.H. Jermyn, Unsupervised image segmentation via Markov trees and complex wavelets, in: Proceedings of IEEE International Conference on Image Processing (ICIP'02), vol. 3, 2002, pp. 801–804.

[17] F. Yan, L. Cheng, S. Peng, Dual-tree complex wavelet hidden Markov tree model for image denoising, Electronics Letters 43 (2007) 973–975.

[18] S. Rahman, M. Ahmad, M. Swamy, Statistics of 2D DT-CWT Coefficients for a Gaussian Distributed Signal, IEEE Transactions on Circuits and Systems I: Regular Papers 55 (7) (2008) 2013–2025.

[19] T.T. Nguyen, S. Oraintara, The shiftable complex directional pyramid Part 1: theoretical aspects, IEEE Transactions on Signal Processing 56 (10) (2008) 4651–4660.

[20] T.T. Nguyen, H. Chauris, Uniform discrete curvelet transform for seismic processing, in: EAGE Conference and Exhibition (EAGE'08), 2008, pp. 5495–5498.

[21] J.K. Romberg, H. Choi, R.G. Baraniuk, Multiscale edge grammars for complex wavelet transforms, in: Proceedings of IEEE International Conference on Image Processing (ICIP'01), vol. 1, 2001, pp. 614–617.

[22] G. Hua, M.T. Orchard, Image inpainting based on geometrical modeling of complex wavelet coefficients, in: Proceedings of IEEE International Conference on Image Processing (ICIP'07), vol. 1, 2007, pp. 553–556.

[23] G. Hua, M.T. Orchard, Image reconstruction from the phase or magnitude of its complex wavelet transform, in: Proceedings of IEEE International Conference on Acoustics, Speech and Signal Processing (ICASSP'08), 2008, pp. 3261–3264.

[24] Z. Wang, E.P. Simoncelli, Local phase coherence and the perception of blur, Advances in Neural Information Processing Systems, vol. 16, MIT Press, Cambridge, MA, 2004, pp. 786–792.

[25] R. Anderson, N. Kingsbury, J. Fauqueur, Coarse-level object recognition using interlevel products of complex wavelets, in:

Proceedings of IEEE International Conference on Image Processing (ICIP'05), vol. 1, 2005, pp. 3066–3077.
[26] X. Zhang, Y. Jia, Face recognition with local steerable phase feature, Pattern Recognition Letters 27 (16) (2006) 1927–1933.
[27] M. Miller, N. Kingsbury, Statistical image modelling using interscale phase relationships of complex wavelet coefficients, in: Proceedings of IEEE International Conference on Acoustics, Speech and Signal Processing (ICASSP'06), vol. 2, 2006, pp. II-789–II-792.
[28] J.F. Ryan Anderson, N. Kingsbury, Determining multiscale image feature angles from complex wavelet phases, in: Proceedings of International Conference on Image Analysis and Recognition (ICIAR), 2005, pp. 490–498.
[29] I.W. Selesnick, R.G. Baraniuk, N.C. Kingsbury, The dual-tree complex wavelet transform, IEEE Signal Processing Magazine 22 (6) (2005) 123–151.
[30] B. Wang, Y. Wang, I. Selesnick, A. Vetro, Video coding using 3-D dualtree discrete wavelet transforms, in: Proceedings of IEEE International Conference on Acoustics, Speech, and Signal Processing (ICASSP)'05, vol. 2, 2005, pp. 61–64.
[31] A. Vo, T.T. Nguyen, S. Oraintara, Image denoising using shiftable directional pyramid and scale mixtures of complex Gaussians, in: Proceedings of IEEE International Symposium on Circuits and Systems (ISCAS'07), 2007, pp. 4000–4003.
[32] J. Magarey, N. Kingsbury, Motion estimation using a complex-valued wavelet transform, IEEE Transactions on Signal Processing 46 (4) (1998) 1069–1084.
[33] Z. Wang, E. Simoncelli, Translation insensitive image similarity in complex wavelet domain, in: Proceedings of IEEE International Conference on Acoustics, Speech, and Signal Processing (ICASSP'05), vol. 2, 2005, pp. 573–576.
[34] A. Vo, T.T. Nguyen, S. Oraintara, Texture image retrieval using complex directional filter bank, in: Proceedings of IEEE International Symposium on Circuits and Systems (ISCAS'06), 2006, pp. 5495–5498.
[35] N. Kingsbury, Image processing with complex wavelets, Philosophical Transactions on Royal Society London A 357 (1760) (1999) 2543–2560.
[36] N. Kingsbury, Complex wavelets for shift invariant analysis and filtering of signals, Journal of Applied and Computational Harmonic Analysis 10 (3) (2001) 234–253.
[37] Y.P. Lin, P.P. Vaidyanathan, Theory and design of two-dimensional filter banks: a review, Multidimensional Systems and Signal Processing 7 (3–4) (1996) 263–330.
[38] E.P. Simoncelli, W.T. Freeman, E.H. Adelson, D.J. Heeger, Shiftable multiscale transform, IEEE Transactions on Information Theory 38 (2) (1992) 587–607.
[39] E. Candès, L. Demanet, D. Donoho, L. Ying, Fast discrete curvelet transforms, Multiscale Modeling Simulation 5 (3) (2006) 861–899.
[40] K.V. Mardia, P.E. Jupp, Directional Statistics, Wiley, New York, 2000.
[41] S. Jammalamadaka, A. SenGupta, Topics in Circular Statistics, World Scientific, Singapore, 2001.
[42] B. Manjunath, W. Ma, Texture features for browsing and retrieval of image data, IEEE Transactions on Pattern Analysis and Machine Intelligence 18 (8) (1996) 837–842.
[43] M. Kokare, P.K. Biswas, B.N. Chatterji, Texture image retrieval using new rotated complex wavelet filters, IEEE Transactions on Systems, Man, and Cybernetics 35 (6) (2005) 1168–1178.
[44] M.N. Do, M. Vetterli, Wavelet-based texture retrieval using generalized Gaussian density and Kullback–Leibler distance, IEEE Transactions on Image Processing 11 (2) (2002) 146–158.
[45] M.N. Do, M. Vetterli, Rotation invariant texture characterization and retrieval using steerable wavelet-domain hidden Markov models, IEEE Transactions on Multimedia 4 (4) (2002) 517–527.
[46] T. Randen, J.H. Husøy, Multichannel filtering for image texture segmentation, Optical Engineering 33 (8) (1994) 2617–2625.
[47] T. Randen, J.H. Husøy, Filtering for texture classification: a comparative study, IEEE Transactions on Pattern Analysis and Machine Intelligence 21 (4) (1999) 291–310.
[48] A.C. Bovik, M. Clark, W.S. Geisler, Multichannel texture analysis using localized spatial filters, IEEE Transactions on Pattern Analysis and Machine Intelligence 12 (1) (1990) 55–73.
[49] A.K. Jain, F. Farrokhnia, Unsupervised texture segmentation using Gabor filters, Pattern recognition 24 (12) (1991) 1167–1186.
[50] D. Dunn, W.E. Higgins, J. Wakeley, Texture segmentation using 2-D Gabor elementary functions, IEEE Transactions on Pattern Analysis and Machine Intelligence 16 (2) (1994) 130–149.
[51] S. Krishnamachari, R. Chellappa, Multiresolution Gauss–Markov random field models for texture segmentation, IEEE Transactions on Image Processing 6 (2) (1997) 251–267.
[52] H. Choi, R.G. Baraniuk, Multiscale image segmentation using wavelet-domain hidden Markov models, IEEE Transactions on Image Processing 10 (9) (2001) 1309–1321.
[53] Y. Xia, D. Feng, R. Zhao, Adaptive segmentation of textured images by using the coupled Markov random field model, IEEE Transactions on Image Processing 15 (11) (2006) 3559–3566.
[54] D. Charalampidis, T. Kasparis, Wavelet-based rotational invariant roughness features for texture classification and segmentation, IEEE Transactions on Image Processing 11 (8) (2002) 825–837.
[55] K.-H. Liang, T. Tjahjadi, Adaptive scale fixing for multiscale texture segmentation, IEEE Transactions on Image Processing 15 (1) (2006) 249–256.
[56] X. Liu, D. Wang, Image and texture segmentation using local spectral histograms, IEEE Transactions on Image Processing 15 (10) (2006) 3066–3077.
[57] P. Brodatz, A Photographic Album for Artists and Designers, Dover, New York, 1966.
[58] M. Unser, Texture classification and segmentation using wavelet frames, IEEE Transactions on Image Processing 4 (11) (1995) 1549–1560.